Stochastic 3D modeling of Ostwald ripening at ultra-high volume fractions of the coarsening phase

A. Spettl[1], R. Wimmer[1], T. Werz[2], M. Heinze[3], S. Odenbach[3], C. E. Krill III[2] and V. Schmidt[1]

[1]Institute of Stochastics, Ulm University, Germany
[2]Institute of Micro and Nanomaterials, Ulm University, Germany
[3]Institute of Fluid Mechanics, TU Dresden, Germany

E-mail: `aaron.spettl@uni-ulm.de`

Abstract. We present a (dynamic) stochastic simulation model for 3D grain morphologies undergoing a grain coarsening phenomenon known as Ostwald ripening. For low volume fractions of the coarsening phase, the classical LSW theory predicts a power-law evolution of the mean particle size and convergence toward self-similarity of the particle size distribution; experiments suggest that this behavior holds also for high volume fractions. In the present work, we have analyzed 3D images that were recorded *in situ* over time in semisolid Al-Cu alloys manifesting ultra-high volume fractions of the coarsening (solid) phase. Using this information we developed a stochastic simulation model for the 3D morphology of the coarsening grains at arbitrary time steps. Our stochastic model is based on random Laguerre tessellations and is by definition self-similar—*i.e.,* it depends only on the mean particle diameter, which in turn can be estimated at each point in time. For a given mean diameter, the stochastic model requires only three additional scalar parameters, which influence the distribution of particle sizes and their shapes. An evaluation shows that even with this minimal information the stochastic model yields an excellent representation of the statistical properties of the experimental data.

Keywords: Grain coarsening, Ostwald ripening, stochastic model, Laguerre tessellation

Submitted to: *Modelling Simul. Mater. Sci. Eng.*

PACS numbers: 02.70.Rr, 07.05.Tp, 81.05.Bx

1. Introduction

Ostwald ripening is a phenomenon that can occur when particles of a given phase are embedded in a matrix consisting of a second phase: in order to reduce the excess energy of interphase boundaries, larger particles tend to grow at the expense of smaller ones, which eventually disappear completely. An introduction to this topic and a review of existing theories may be found in *e.g.* [1–6]. In the limit of low volume fractions V_V of the coarsening phase ($V_V \rightarrow 0$), the classical LSW theory [7, 8] predicts a power-law evolution of the mean particle size and convergence toward self-similarity of the particle size distribution. In this regime, it is acceptable to approximate the coarsening particles as isolated domains embedded in a homogeneous matrix. At higher volume fractions, however, such a simplification is no longer tenable [9]. There, particle-particle interactions and correlations become significant [10–12], and the local geometry of particle boundaries exerts a strong influence on the resulting kinetics [13, 14]. Despite many decades of research into the phenomenon of Ostwald ripening, there is still much to be learned about coarsening in the high-V_V limit. Recent efforts in this regard include experimental investigations [15–18], phase-field and Monte-Carlo simulations [19–22] as well as analytic modeling [23, 24].

Modeling approaches that are designed to capture the statistical properties of a multiparticle microstructure can potentially contribute deeper insight into the morphology and dynamics of systems undergoing Ostwald ripening. This ought to be particularly true for simple parametric models of particle morphology, as the limited number of parameters makes them amenable to individual physical interpretation. A first step in the development of such a parametric model—and a primary goal of this paper—is therefore to extract the essential statistical properties of coarsening particle systems from experimental data. We perceive the particle systems to be realizations of random sets of particles, and we postulate that the properties of these (sets of) random particles can be represented by a simple and parametric stochastic model.

One potential application for such stochastic models is their integration into multiscale computational models, which aim to span a wide range of lengths and/or times by the judicious combination of individual models optimized for different length/time scales. This is the strategy behind Integrated Computational Materials Engineering (ICME) [25] for the computer-based design of new materials and their requisite processing techniques. Frequently, for the adequate simulation of a given materials processing step, it is not necessary to compute the actual migration of individual grain or phase boundaries; rather, it suffices to capture the resulting change in microstructure in a purely statistical sense. By generating a 3D microstructure with appropriate structural properties from a statistical model, one can readily "populate" the sample space simulated by a macroscopic model operating at much longer length scales, thereby vastly improving the overall computational efficiency of the multiscale model. Once this step has been carried out, a representative volume can be carved out as the basis for computing any relevant microsctructure-dependent properties, which can then be fed back in to the macroscopic model.

Based on this motivation, we develop a (dynamic) stochastic simulation model that describes the particle morphology of a two-phase multiparticle system in which the coarsening phase occupies an ultra-high volume fraction, $V_V \geq 0.9$, of the sample. (For the experimental data set to which we apply the model, we have $V_V = 0.93$.) The model is based on random Laguerre tessellations, with each (convex) cell of the tessellation representing a region containing exactly one particle. We implement the dynamics of coarsening such that the mean particle size $\bar{R}(t)$ follows a power law of the form

$$\bar{R}^n(t) - \bar{R}^n(0) = k \cdot t, \quad t > 0, \tag{1}$$

where the scaling exponent $n > 0$ takes on a value that is determined by the underlying mechanism for coarsening [3], $k > 0$ depends on the kinetics operating in the material, and $\bar{R}(0)$ denotes the mean particle size at the initial time $t = 0$. We note that the scaling exponent has been the subject of considerable discussion in the literature: at low to fairly high volume fractions of the coarsening phase, a value of $n = 3$ has been reported to hold not only in experimental investigations of Ostwald ripening [16, 26] but also in computer simulations [21] and analytic modeling [2, 5]. The situation is murkier, however, in the ultra-high volume fraction regime ($0.9 \lesssim V_V < 1$), where comparatively few studies [19, 27–29] have been performed. According to [19], a scaling parameter $n = 3$ is suitable up to $V_V = 0.96$, as the kinetics of phase coarsening is still approximately controlled by diffusion through the matrix. This conclusion is consistent with the experimental data analyzed in [27]. But there have also been reports of scaling exponent values as low as 2.6 and as high as 4 (see *e.g.* [28, 29]), depending on the particular growth scenario.

In addition to power-law growth, we assume the particle size distribution that is generated by Ostwald ripening to be *self-similar,* meaning that a simple rescaling transforms the distributions at arbitrary times into each other. More formally, we call the family $\{R(t), t \geq 0\}$ of (random) particle sizes self-similar if their cumulative distribution functions $F_{R(t)}$, $t \geq 0$, fulfill the relationship

$$F_{R(t)}\left(x/\bar{R}(t)\right) = F_{R(0)}\left(x/\bar{R}(0)\right), \quad x \in \mathbb{R},$$

with $\bar{R}(t)$ equal to the expectation value $\mathbb{E}[R(t)]$. Once again, although experiments generally support a tendency for convergence toward a self-similar distribution, there has been considerable debate regarding the question of whether the self-similar state is reached in finite time in real systems [30, 31]. In this work, we adopt the pragmatic approach of applying our model to experimental data for which any time-dependent variations in the shape of the size distribution are smaller than the latter's statistical uncertainty.

The model is fitted to experimental X-ray tomographic datasets obtained at the European Synchrotron Radiation Facility (ESRF) in Grenoble. Tomographic scans of 24 sec duration were performed repeatedly on an Al-5 wt% Cu alloy sample held at

592 °C, thereby producing a two-phase microstructure of solid particles embedded in a liquid matrix. At this temperature, the liquid phase constitutes only 7% of the sample by volume, and the microstructural dynamics are slow enough that each tomographic scan can be considered to be a snapshot of the instantaneous state of the system. Armed with a series of time steps spanning more than 800 min, we employ a fitting procedure to several time steps in order to fix the values of the model parameters, and then we use an additional time step for model validation. We find that our model fits the experimental data quite well, which is rather remarkable, considering that close agreement means that a completely random and time-dependent microstructure has been described statistically with only six parameters: three for the dynamics of particle coarsening (Eq. (1)) and another three for the full 3D morphology of the particles and their size distribution.

This paper is structured as follows: In Section 2 we describe the experimental samples, the tomographic imaging technique and the data processing steps. In particular, we explain how the tomographic reconstructions were segmented structurally—a procedure that entailed the detection of individual particles and their representation as convex polyhedra. Our stochastic model is introduced in Sections 3 and 4. First, in Section 3, we describe the underlying (static) 3D model, which is able to capture the morphology of 3D grain microstructures at any fixed point in time using 3D tessellations consisting of convex cells. This model is parametric in nature and can be fitted to any coarsening state; consequently, it is able to represent grain microstructures at any scale. Secondly, in Section 4, we construct a *time function* that maps from the coarsening state—*e.g.,* the duration of annealing—to the 3D model parameters. This function adheres to the power-law growth of grains, ensures self-similarity and is also parametric. The 3D model considered together with the time function for describing system dynamics constitutes the *dynamic model.* In Section 5, the proposed dynamic model is fitted to experimental (time-resolved) data. We validate the dynamic model using various characteristics estimated from experimental and simulated data. Finally, in Section 6, we summarize the results and provide an outlook for future work.

2. Experimental data, imaging and segmentation

In this section we describe the experimental sample, the 3D imaging technique and the steps performed during image processing, paying particular attention to the segmentation of tomographic data sets, which was carried out according to well-known techniques [32, 33]. Binarization of the tomographic reconstructions yielded images with incompletely marked particle boundaries. The watershed algorithm [34–37] was therefore employed to detect basins in which single particles were located. A postprocessing step removed the remaining segmentation artifacts, based on the assumption of approximate convexity of particles. Finally, we extracted convex polyhedra from the experimental data as representations of individual particles, which significantly facilitates the computation of particle characteristics during subsequent stages of data analysis.

2.1. Experimental sample and in situ 3D imaging

To obtain three-dimensional data for a microstructure undergoing Ostwald ripening at a high volume fraction of the coarsening phase, we studied a cylindrical sample of Al-5 wt% Cu. The constituent material had been homogenized at 500 °C for 24 hours in air and subsequently cold-rolled to a thickness reduction of 50%. Finally the sample was cut by spark erosion into cylinders 8.5 mm in length and 4 mm in diameter. A custom-built furnace that was designed to be compatible with the spatial and optical constraints of beamline ID15A at ESRF allowed for the time-resolved *in situ* measurement of coarsening processes in the semisolid state of the sample at a temperature of 592 °C. Application of the lever rule to the Al–Cu phase diagram [38] yields a volume fraction of the solid (coarsening) phase of $V_V = 0.93$ at thermodynamic equilibrium between the solid and liquid. Owing to the higher concentration of Cu dissolved in the liquid phase at this temperature (22.4 vs. only 3.5 wt% in the solid phase) the liquid matrix absorbs X-rays more strongly than the coarsening particles do, which enables absorption-contrast tomography to map out the matrix phase. Absorption images were recorded at a beam energy of 47.4 keV. A tomographic scan was performed every 10 minutes over the course of 25 hours, with each scan consisting of 8000 projections recorded within an individual scan time of 24 sec. All tomographic reconstructions were generated by the standard filtered backprojection technique from the projection series, and the nominal resolution of the final reconstructed data is given by the voxel side length of 5.36 µm.

In the following, we denote an image I that corresponds to an individual tomographic dataset by $\{I(x,y,z) \in \{0,\dots,255\} : (x,y,z) \in W\}$, where $W \subset \mathbb{N}^3$ is the grid of voxel coordinates and the possible grayscale values are given by $\{0,\dots,255\}$. The reconstructed images are denoted by I_t, with the index t indicating the annealing duration. In this work, we examined the datasets that were recorded at annealing times of $t = 200$, 400, 600, 750, 900 and 1000 min. It should be noted that, in a previous study of Ostwald ripening in Al-Cu with $V_V = 0.74$, the particle size distribution was found to evolve in a (nearly) self-similar manner after about 3 hours of annealing [18]. Therefore, the earliest time step analyzed was $t = 200$ min. Although we cannot be sure that our sample has reached steady-state conditions by this time, even in the case of a very slowly evolving transient state of the sample, it makes sense to represent the structural features using a stochastic model. Naturally, in that case, predictability is limited to the time spanned by the experiment.

2.2. Ring artifacts

An important preprocessing step is the removal of ring artifacts, which are often present in tomographic reconstructions. We have carried out this correction based on the approach presented in [39]. Images that have been subjected to ring-correction are denoted by a prime, as in I'_t. Figure 1 shows a slice through a tomographic reconstruction before and after ring correction.

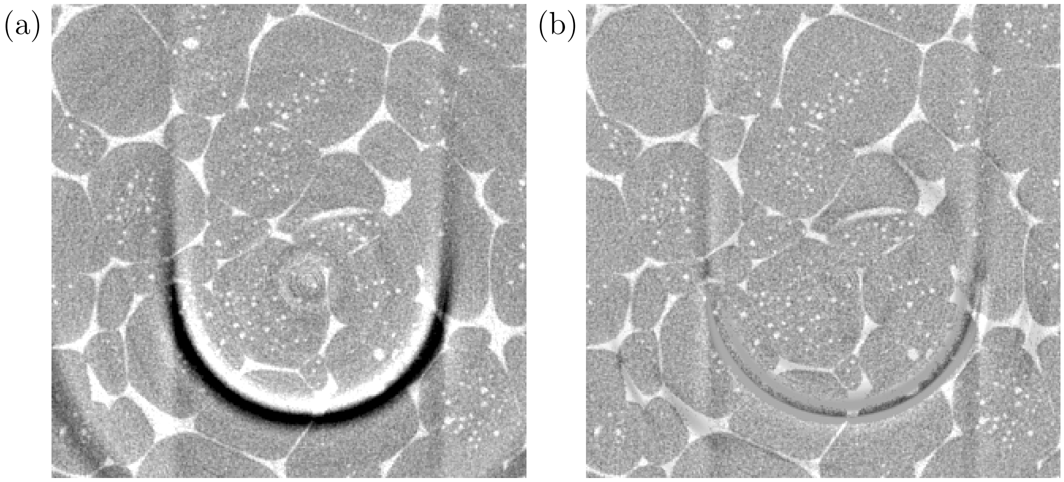

Figure 1. Slice through a tomographic data set before and after correction for ring artifacts. Note that the regions of greatest distortion are not corrected completely, but even in such locations the quality of the resulting image suffices for subsequent segmentation steps.

2.3. Binarization

Global thresholding of the grayscale image I_t' shown in Figure 1(b) yields binary images B_t with incompletely marked particle boundaries, as depicted in Figure 2(a). In addition, numerous small white objects are visible in B_t, which indicate the presence of liquid droplets enclosed within the solid phase; these should not be confused with the network of particle boundaries. Therefore, we first apply the Hoshen-Kopelman algorithm [40] to detect connected (white) components in the images. Entrapped liquid drops can be recognized by their comparatively small volume, and they are removed based upon this criterion (using a manually chosen threshold value). The remaining (incomplete) particle boundaries are dilated using a sphere $b(o, 3)$ centered at the origin o with radius 3 as structuring element. This step closes small gaps and reduces the frequency of oversegmentation during subsequent segmentation steps. Binary images that have been preprocessed in this manner—see Figure 2(b) for a visualization—are denoted by B_t'.

2.4. Watershed transformation

The particle boundaries visible in the binary images B_t' are incompletely marked. To rectify this unsatisfactory situation, we employ the watershed transformation [34–37], which operates on the interpretation of grayscale values in an image as denoting a local "height" above ground level. The local minima (that is, the "valleys") in this landscape are then progressively flooded with water—*i.e.*, every local minimum generates a region that grows during the flooding procedure. At locations of impingement between growing regions, a *watershed* curve (in 2D) or surface (in 3D) is placed, which prevents further growth of the adjacent regions in the direction perpendicular to the watershed.

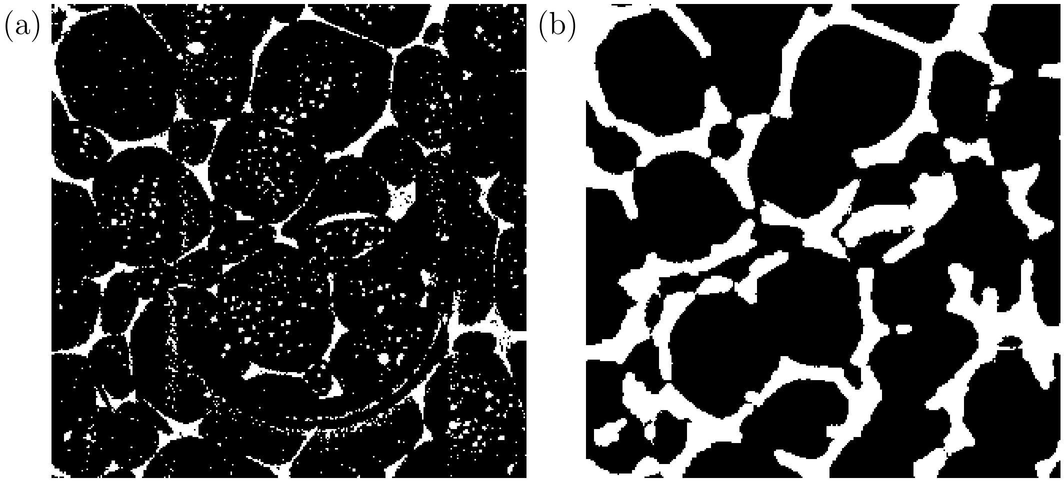

Figure 2. Image processing of Figure 1(b) following (a) binarization and (b) removal of entrapped liquid drops and subsequent dilation.

Application of the (inverted) Euclidean distance transform [32] to B'_t images generates suitable grayscale input for the watershed transformation. At each voxel in the solid (black) phase of B'_t, the distance transform D_t specifies the shortest distance to a voxel of the liquid (white) phase. Following inversion of these D_t values, the local minima in the resulting mapping correspond to voxels located furthest from the known (incompletely marked) particle boundaries.

One problem with the conventional watershed transformation is oversegmentation (*i.e.,* the generation of spurious additional regions). The Euclidean distance transform is quite sensitive to small artifacts in the binary image, which then carry over to the detection of local minima and, subsequently, to the computed watershed locations. One approach toward minimizing this problem is to apply a marker-based watershed algorithm, in which the flooding process is begun not from each local minimum in the plot of the inverse distance transform but only from a predefined set of markers. To place such markers in our data, we first generalize the concept of a (regional) local minimum. A (regional) local minimum is identified as a connected set of voxels having (the same) grayscale value that is smaller than the grayscale values in their direct neighborhood. These grayscale values are obtained from the image where the flooding is performed, *i.e.*, the inverted distance transform in this case. We define an *extended regional minimum* to contain the voxels of the regional minimum plus all adjacent voxels having grayscale values that differ by no more than $\varepsilon \geq 0$ from the grayscale value of the regional minimum. When constructing the extended regional minimum, we apply the additional constraint that watershed boundaries may never be crossed; in other words, an extended regional minimum is not permitted to extend into adjacent watershed regions (which are obtained from computing the watershed transform based on (standard) regional minima). This procedure alone has no influence on oversegmentation, as the number of regions remains unchanged. The key step in reducing the generation of spurious watersheds is the following: whenever two extended regional minima meet at a watershed

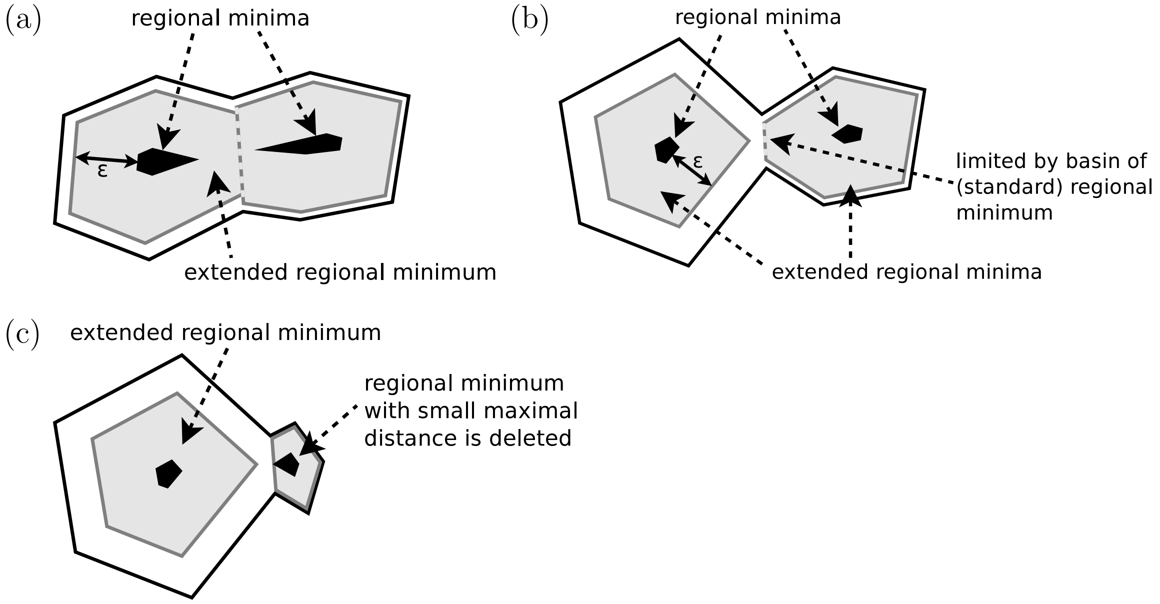

Figure 3. Schematic illustration of extended regional minima as markers for the watershed algorithm: (a) two extended regional minima meet at a watershed and will therefore be joined together; (b) two extended regional minima that will not be joined, as they do not make contact at a watershed; (c) (extended) regional minima located in very small cells are deleted.

boundary, they are joined together, as illustrated in Figure 3(a). This has the effect that mainly adjacent regions are merged when they are both small, whereby not only their size is considered but also their shape. If only one of the neighboring extended regional minima touches a watershed, however, the two regions are not joined together (Figure 3(b)). Furthermore, (extended) regional minima belonging to very small cells (which can be detected by their small (maximum) distance value to the nearest particle boundary voxel) are deleted (Figure 3(c)). This avoids very small cells in the final segmentation. Note that from the illustration in Figure 3(a) it is not clear that joining the two regions is preferable to leaving them apart, but in 3D there are more cases where the distance transform is disturbed in a similar way and joining the regions is required to avoid oversegmentation.

The result of the marker-based watershed transformation based on extended regional minima is a new binary image with completed grain boundaries, which we call B''_t (Figure 4(a)). When segmenting our data, we obtained good results using $\varepsilon = 5$ voxels.

2.5. Postprocessing

As can be seen in Figure 4(a), the marker-based watershed algorithm does not eliminate all instances of oversegmentation, as there are obvious problems with small "particles" appearing along boundaries that were poorly marked in the original tomographic reconstruction. These spurious particles can be identified by the fact that they appear

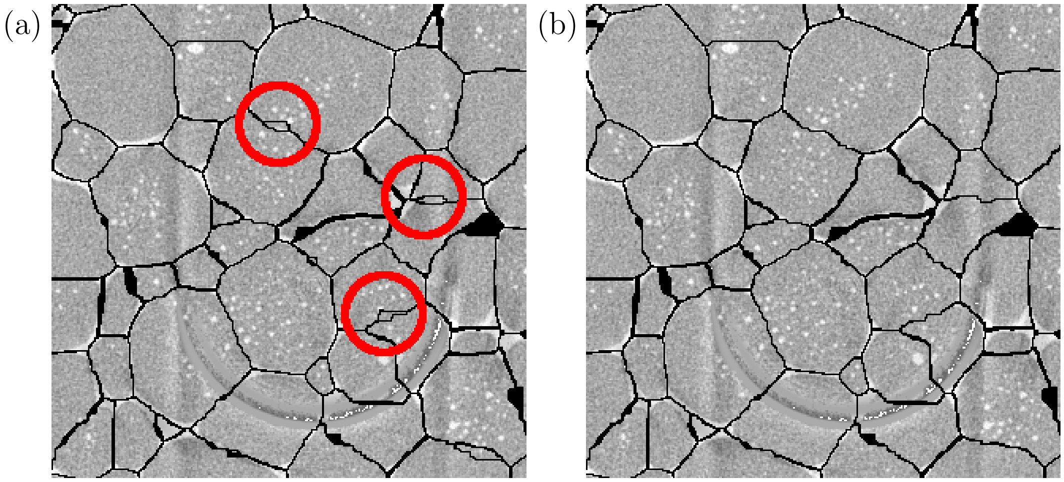

Figure 4. Image processing of Figure 1(b) following the steps illustrated in Figure 2. (a) The marker-based watershed transformation, with remaining segmentation artifacts marked by red circles; (b) after further postprocessing to remove the excessive overlap of particle convex hulls. Both binary images are superimposed on the original grayscale data.

to have been "carved out" of a larger adjacent particle. We express this criterion in mathematical terms by noting that the particles in our sample are approximately convex in shape: consequently, by computing the convex hull for all particles and determining the extent to which a given particle is covered by the convex hull of a neighbor, we can unambiguously identify a spurious particle as one whose overlap with a neighbor's convex hull exceeds a threshold of 40 %. In that case, the spurious particle is deleted and its volume is added to the neighbor (Figure 4(b)).

The postprocessed binary images are denoted by B_t'''. The detection of connected components yields a labeled image L_t given by $\{L_t(x, y, z) \in \{0, \ldots, N_t\} : (x, y, z) \in W\}$, in which the value $L_t(x, y, z) \in \{1, \ldots, N_t\}$ denotes the particle number, N_t is the total number of particles at time t, and $L_t(x, y, z) = 0$ corresponds to particle boundaries (with a thickness of one voxel in 3D, which may appear thicker in 2D cross-sections). From the information contained in L_t, we can perform statistical analyses of the particle regions $R_t(i) = \{(x, y, z) \in W : L_t(x, y, z) = i\}, i = 1, \ldots, N_t,$.

2.6. Extraction of convex polyhedra

Some characteristics of particles are difficult to estimate directly from voxelated data. Therefore, we apply the algorithm presented in [41] to extract convex polyhedra from experimental image data using orthogonal regression. The system of particles $\{R_t(i), i = 1, \ldots, N_t\}$ is described by a set of convex polyhedra $\{C_t(i), i = 1, \ldots, N_t\}$, from which various characteristics can be readily computed. Furthermore, such polyhedra are a more realistic target for modeling than are the experimentally measured particles, as the latter need not be perfectly convex—*i.e.*, their faces and edges can be slightly curved. In the stochastic model presented in Section 3, we consider only the case of a space-filling ensemble of convex grains. This means that each simulated grain must have the shape of a convex polyhedron (that is, all of its faces must be planar). For a sensible comparison of characteristics computed from such a model to those extracted from experiment, we must first determine a “best fit” representation of the experimental data using convex polyhedra in order to maintain consistency with the assumptions underlying the modeling.

Note that tomographic reconstructions and their structural segmentation are discussed again in Section 5, where the proposed dynamic simulation model is fitted to and validated against experimental data. In the next two sections, our stochastic modeling approach is presented.

3. Stochastic 3D microstructure model

In this section we introduce a stochastic simulation model for the particle morphologies observed during Ostwald ripening. We consider only the case of an ultra-high volume fraction of the coarsening phase, which means that particles fill space almost completely; for this reason, we alternatively refer to particles as *grains*, as this is the standard terminology in materials science for the constituent elements of a single-phase polycrystalline microstructure. Owing to the space-filling arrangement of such grains, it is natural to model the resulting microstructures using tessellations. By definition, a tessellation divides space into disjoint regions, usually called *cells*. To begin with, we attempt to describe the instantaneous state of such a microstructure by means of a stochastic tessellation model computed in three dimensions.

First, we introduce the notion of a Laguerre tessellation, which is the mathematical basis of our modeling approach. Then, we extend the (deterministic) Laguerre tessellation with the help of a random weighted point pattern to a stochastic model, which leads to the concept of a random Laguerre tessellation [42].

3.1. Laguerre tessellations

A generalization of the well-known Voronoi diagram is the *Laguerre tessellation* [43]. Like standard Voronoi diagrams, Laguerre tessellations consist of convex cells (*i.e.*, convex polyhedra), but additional weights are used to control cell sizes. Because Laguerre tessellations are easy to define, they are attractive for modeling grain microstructures. For example, polycrystalline structures have been modeled with the help of Laguerre tessellations in [44–48]. Furthermore, Laguerre tessellations have been applied to the stochastic modeling of other materials, too, *e.g.* open and closed-cell foams [49, 50].

Formally, a 3D Laguerre tessellation is defined as follows. Given a (locally finite) set $S = \{(\mathbf{x}_i, r_i), i \in I\} \subset \mathbb{R}^3 \times \mathbb{R}^+$ of *seed points* $\mathbf{x}_i \in \mathbb{R}^3$ (also called *spring points* or *generators*) with indices in some (finite or countable) set I and weights $r_i \geq 0$, the

Laguerre cell of $(\mathbf{x}_i, r_i)$ with respect to S is given by

$$C\left((\mathbf{x}_i, r_i), S\right) = \left\{\mathbf{y} \in \mathbb{R}^3 : |\mathbf{y} - \mathbf{x}_i|^2 - r_i^2 \leq |\mathbf{y} - \mathbf{x}_j|^2 - r_j^2,\ (\mathbf{x}_j, r_j) \in S,\ j \neq i\right\} \ .$$

Then, the Laguerre tessellation is the set of all Laguerre cells $\{C((\mathbf{x}_i, r_i), S), i \in I\}$. The weights r_i allow control over cell sizes and can be interpreted as the radii of spheres centered at the seed points (see Figure 5 for an illustration in 2D). Note that it is possible for a seed point to create no cell at all, provided an adjacent seed point has a sufficiently large weight. For the same reason it is possible for a seed point not to be contained within the cell generated by that seed point.

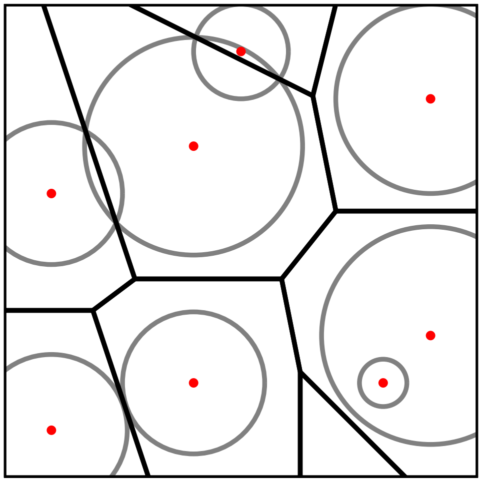

Figure 5. Illustration of a Laguerre tessellation in 2D: seed points with weights pictured as circles, along with the resulting Laguerre cell boundaries.

It may come as a surprise to learn that every *normal* tessellation in 3D that consists entirely of convex cells is a Laguerre tessellation [42]. A normal tessellation is one in which neighboring cells have coinciding faces, edges and vertices (*face-to-face* property); furthermore, each planar face borders exactly two cells, each edge belongs to exactly three cells and each vertex is shared by exactly four cells. Since these conditions are typically satisfied by real polycrystalline microstructures, Laguerre tessellations are a natural choice for modeling polycrystalline materials. Note that real grains are usually only approximately convex, but we do not consider the slight curvatures of their faces in this paper; instead, we approximate all faces by planar regions and all edges by straight line segments.

3.2. Random weighted point pattern by sphere packing

In order to model a polycrystalline material by means of a Laguerre tessellation, we must choose appropriate input parameters such that the resulting tessellation reflects the characteristics of the real microstructure. One approach to generating the set $S = \{(\mathbf{x}_i, r_i), i \in I\}$ of seed points and weights would be to employ a random point process—for example, a Poisson process to determine seed locations and independent,

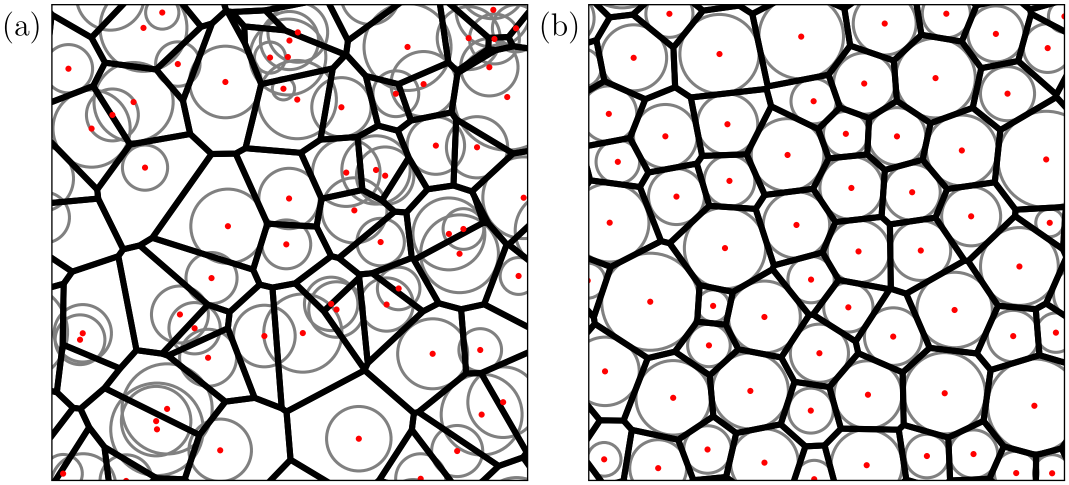

Figure 6. Realizations of random Laguerre tessellations in 2D: (a) seed points with independently generated locations (Poisson-Laguerre tessellation with gamma-distributed weights), and (b) with nearly no overlap of weighting circles, which generates a more regular arrangement of cells.

identically distributed random variables to fix the weights—in order to obtain a random marked point pattern [51–54]. However, our investigations have found that real polycrystalline microstructures are in a sense "too regular" for this approach to yield acceptable results, as simple random point process models generate broader distributions of cell topologies and sizes than those measured experimentally. This issue is illustrated in Figure 6, where it can be observed that shifting the seed locations to reduce the overlap of weighting circles (*i.e.,* imposing a non-random modification on the marked point pattern) produces a much more realistic ensemble of Laguerre cells. For this reason, we take an alternative approach to generating the marked point pattern of seed points and their weights.

Random sphere packings are often used to model systems of (spherical) particles, and such packings are well suited to specifying the locations of (weighted) seed points [44, 55]. A random sphere packing is an arrangement of non-overlapping spheres with a packing density $d \in [d_{\min}, d_{\max}]$, with $d_{\min} \approx 0.5$ and $d_{\max} \approx 0.65$. Note that for packing densities $d > 0.65$, the arrangement of spheres must be nearly regular for equally sized spheres. For our polycrystalline data, we found that partially overlapping spheres are better suited as (weighted) seed points. For this reason, we will generate sets of moderately overlapping spheres from a dense packing of "hard cores," which are themselves spherical in shape and fixed concentrically within the overlapping spheres.

One common approach to packing spheres is to employ so-called *collective-rearrangement algorithms* [56], which repeatedly displace individual spheres with the aim of reducing and finally eliminating sphere overlap. For example, the *force-biased algorithm* [57, 58] is a popular collective-rearrangement algorithm, which we use during simulations restricted to a bounded window (Section 3.3). However, first we introduce a stochastic model for sphere packings defined on $\mathbb{R}^3$—*i.e.,* a stationary model that is not restricted to (bounded) subsets of $\mathbb{R}^3$.

The idea of (stationary) random sphere packing models in $\mathbb{R}^m$, $m \geq 2$, is described in [59]. Based on a (locally finite) stationary point process involving *e.g.* spheres (with random radii) as marks and a given collective-rearrangement rule, conditions can be formulated such that iterative application leads to convergence to a non-overlapping and stationary (random) system of spheres. In particular, for sets of spheres an avoidance algorithm can be determined, which is a minor modification of the force-biased algorithm and leads to the same results in practice. For our stochastic model, we use exactly this technique. A homogeneous Poisson process with intensity $\lambda > 0$ gives us the initial random configuration of points, and points are independently marked with spheres following a chosen distribution for the radii, *i.e.*, radii are drawn from independent copies of a random sphere radius $R_{\text{sphere}} > 0$. We assume that each sphere contains a hard-core region in which no overlap with other hard-core regions is permitted. The radius of each hard core is computed by applying a (constant) scaling factor $s_{\text{hc}} \in (0, 1]$ to the corresponding sphere radius. The avoidance algorithm rearranges the set of hard cores to remove overlap. Note that for a given sphere radius distribution (of the random variable R_{sphere}) and a given value for the scaling parameter s_{hc}, the intensity λ and packing density d_{hc} (with respect to the hard cores) are related to each other through the relation

$$d_{\text{hc}} = \lambda \cdot \mathbb{E}\left(\frac{4}{3}\pi(s_{\text{hc}} \cdot R_{\text{sphere}})^3\right) ,$$

which assumes that sphere radii are not modified by the collective-rearrangement algorithm. Furthermore, we denote by $d = d_{\text{hc}}/s_{\text{hc}}^3$ the expected ratio of the sum of all individual sphere volumes to the volume of the simulation window. It is not a packing density, because, typically, the spheres will overlap (in the case of $s_{\text{hc}} < 1$). However, we will use d instead of d_{hc} in the discussion below, as the meaning of d can be interpreted without making reference to the hard core scaling factor s_{hc}. For example, $d = 1$ means that the volume of all spheres taken together is identical to the overall volume of the simulation window (which suggests that there should be a close relationship between the sphere volume and its generated Laguerre cell volume).

In real polycrystalline microstructures, the grain diameter distribution (computed using equivalent-volume sphere diameters) is often found to have the shape of a log-normal or gamma distribution [60]—*i.e.,* one observes right-skewed distributions. For our experimental data, this effect is only slightly evident. Therefore, we choose the truncated normal distribution for the distribution of sphere radii: $R_{\text{sphere}} \sim N_+(\mu, \sigma^2)$, where the index "+" emphasizes the (natural) constraint $R_{\text{sphere}} > 0$. Note that μ and σ^2 are the parameters of the underlying normal distribution (*i.e.,* without truncation). A remarkable fact is that a certain skewness in the cell size distribution is obtained automatically from the subsequent random packing of spheres, as smaller spheres have a tendency to generate slightly larger cells in comparison to their radius, because in this case the free space between spheres has a larger impact.

3.3. Algorithm for simulation

Given a bounded simulation window $W \subset \mathbb{R}^3$, and the 3D model parameters R_{sphere}, s_{hc} and d introduced in Section 3.2, the algorithm to obtain a realization of our random Laguerre tessellation model has the following steps:

1. Define a suitable cuboid $W_+ \supset W$ to avoid edge effects in W, where an appropriately enlarged W is completely contained in W_+ (*plus-sampling*). In practice, for our case of $R_{\text{sphere}} \sim N_+(\mu, \sigma^2)$, it is suitable to dilate W using a sphere $b(o, \mu + 2\sigma)$ as structuring element, and to take the bounding cuboid of the resulting set.
2. Initialize the set of spheres: $S = \{\}$.
3. Choose the center $\mathbf{x}'$ of a new sphere candidate uniformly inside the simulation window W_+, and draw a realization r' from an independent copy of the random sphere radius R_{sphere}.
4. If $\left(\sum_{(\mathbf{x},r)\in S} \frac{4}{3}\pi r^3 + \frac{4}{3}\pi (r')^3\right) / \operatorname{vol} W_+ \leq d$, then $S = S \cup \{(\mathbf{x}', r')\}$ and repeat beginning with step 3, else proceed with step 5.
5. Apply the *force-biased algorithm* [57, 58] to the set of hard (spherical) cores $S_{\text{hc}} = \{(\mathbf{x}', s_{\text{hc}} \cdot r') : (\mathbf{x}', r') \in S\}$ in the cuboid W_+ with periodic boundaries, which rearranges them iteratively until overlap between hard cores has been eliminated. Subsequently, transfer the new sphere centers from S_{hc} to S.
6. Compute the Laguerre tessellation using the set S as (weighted) seed points; determine the intersection of the cells with W.

Note that the technique used to obtain the initial configuration in steps 3 to 4 does not correspond to a Poisson process directly, because the number of points in W is not Poisson distributed. By definition of the model on the complete space (*i.e.,* $\mathbb{R}^3$) there may be regions with fewer and regions with a greater number of spheres in a given realization before applying the iterative rearrangement algorithm. But, for relatively high packing densities d_{hc}, the rearrangement rule would (with enough iterations) shift spheres from regions with a greater degree of overlap to regions with less overlap. Consequently, even when computed within relatively small windows the final packing density does not vary much with location. Therefore, for a given bounded simulation window, we directly determine the number of spheres required to obtain the desired packing density almost exactly.

3.4. Summary of the stochastic 3D microstructure model

According to the algorithm presented above, we can generate random packings of spheres having hard cores. The sphere radii follow a (truncated) normal distribution. The centers and radii of these spheres are used as weighted seed points for the Laguerre tessellation. In total, this constitutes a stochastic 3D model having 4 parameters: the mean μ and the variance σ^2 of the normal distribution as well as the parameters s_{hc} and d controlling the packing procedure. It is clear that the mean value μ is directly related to the mean size of cells, which depends on the coarsening state. For this reason, the model can be adapted readily to the dynamic process of coarsening, as described in the following section.

4. Dynamic microstructure model

In Section 3, we introduced a stochastic model for (static) polycrystalline microstructures observed at a given point in time. In the present section, we aim to describe Ostwald ripening using an extension of this stochastic model. As Ostwald ripening is a dynamic process, we construct a dynamic stochastic model. In the following, we define a time function that adheres to power-law growth as well as to self-similarity of the particle size distribution (*cf.* Section 1). The time function maps from the annealing time to the parameters of the 3D model. The time function itself is parametric, and it separates the scale-dependent aspects of particle coarsening from the scale-invariant 3D particle morphology.

Obviously, we require the power-law equation for grain growth given in Eq. (1) to obtain the mean particle radius $\bar{R}(t)$ at arbitrary times $t > 0$. The formula has three parameters, $n > 0$, $k > 0$ and $\bar{R}(0) > 0$. If we wish our model to be consistent with Eq. (1), we must determine suitable values for the parameters of the static 3D model introduced in Section 3 at any t such that the mean cell size matches $\bar{R}(t)$. For a fixed coarsening state, the parameters of our stochastic 3D model are $\mu \in \mathbb{R}$ and σ^2 of the (truncated) normal distribution of sphere radii and the packing parameters s_{hc} and d. Any parameters that depend on the scale will have to be adjusted with t, whereas scale-invariant parameters can be treated as constants. As it is clear that s_{hc} and d are scale invariant, we treat them as constants, estimating their values by a fitting procedure. The remaining two parameters, μ and σ^2, determine the overall scale of the final tessellation; together, they establish the value for $\bar{R}(t)$ according to a functional relationship that is to be determined.

4.1. Parametric time function

We define the time function $p : \mathbb{R}^+ \to \mathbb{R}^+ \times \mathbb{R}^+ \times (0,1] \times \mathbb{R}^+$ by setting

$$p(t) = \begin{pmatrix} \mu \\ \sigma^2 \\ s_{\mathrm{hc}} \\ d \end{pmatrix} = \begin{pmatrix} c_\mu \cdot \bar{R}(t) \\ \left(c_\sigma \cdot \bar{R}(t)\right)^2 \\ s_{\mathrm{hc}} \\ d \end{pmatrix} \quad \text{with} \quad \bar{R}^n(t) = \bar{R}^n(0) + k \cdot t,$$

where $c_\mu > 0$, $c_\sigma > 0$, $s_{\mathrm{hc}} \in (0,1]$, $d > 0$, $n > 0$, $k > 0$ and $\bar{R}(0) > 0$ are parameters of the dynamic model. In the event of self-similarity, it is clear that the factors $c_\mu > 0$ and $c_\sigma > 0$ cannot depend on t. Note that the parameter c_μ is not a true parameter of the dynamic model, as it is merely a correction factor needed to obtain the "correct" expectation value; c_μ could be expressed as an (unknown) function of the other scale-invariant parameters—*i.e.*, $c_\mu = c_\mu(c_\sigma, s_{\mathrm{hc}}, d)$. In other words, for a given packing

Table 1. Overview of model parameters and their physical interpretation.

parameter	scale invariant?	physical interpretation
$\bar{R}(0) > 0$		mean particle radius at time $t = 0$
$n > 0$		scaling exponent for coarsening; determined by the mechanism for coarsening ($n = 3$ has been reported for a wide variety of Ostwald ripening systems)
$k > 0$		growth rate constant; governs speed of coarsening kinetics
$c_\mu = c_\mu(c_\sigma, s_{\mathrm{hc}}, d)$	yes	technical parameter; relates μ to the mean particle radius $\bar{R}(t)$ through the relation $\mu = c_\mu \cdot \bar{R}(t)$
$c_\sigma > 0$	yes	determines the standard deviation of the particle radii
$s_{\mathrm{hc}} \in (0, 1]$	yes	scaling factor to obtain the hard core radii; controls the magnitude of overlapping allowed for spheres during the packing procedure
$d > 0$	yes	sum of individual sphere volumes relative to the volume of the simulation window; governs the packing density of hard cores through the relation $d_{\mathrm{hc}} = d \cdot s_{\mathrm{hc}}^3$

scenario and a given shape of the radius distribution, we can estimate the factor c_μ that is required to obtain μ from $\bar{R}(t)$. An overview of these parameters including their physical interpretation is provided in Table 1.

4.2. Self-similarity

It may be asked whether the time function defined above fulfills the criteria for self-similarity—*i.e.,* whether the family of truncated normal distributions of sphere radii is self-similar. Consider a random variable $X \sim N(\mu, \sigma^2)$. The density function of its truncated version Y with $Y > 0$ is given by

$$f_Y(y) = f_X(y \,| X > 0) = \begin{cases} \frac{f_X(y)}{1 - F_X(0)} & \text{if } y > 0, \\ 0 & \text{otherwise} \end{cases},$$

where $F_X(x) = \Phi\left(\frac{x-\mu}{\sigma}\right)$ is the cumulative distribution function of X, and Φ denotes the cumulative distribution function of the standard normal distribution. Consequently, the question is simplified to whether $F_X(0) = \Phi\left(\frac{0-\mu}{\sigma}\right)$ takes on the same value for all time steps (where X, or more precisely, μ and σ are rescaled). If that is the case, then the distribution X will always be truncated at the same quantile—*i.e.,* the shape of the distribution of Y stays the same. By definition of the time function p, we see that in our case, $\Phi\left(\frac{-\mu}{\sigma}\right)$ becomes

$$\Phi\left(\frac{-p(t)_\mu}{\sqrt{p(t)_{\sigma^2}}}\right) = \Phi\left(-\frac{c_\mu \cdot \bar{R}(t)}{c_\sigma \cdot \bar{R}(t)}\right) = \Phi\left(-\frac{c_\mu}{c_\sigma}\right) = \text{const} \ .$$

Therefore, the family of truncated normal distributions $\{R^{(t)}_{\text{sphere}}, t > 0\}$ used to generate radii for the spheres is self-similar.

We wish to emphasize that not only is the particle radius distribution self-similar, but so, too, is the complete family of (random) 3D morphologies generated by this model. This is easy to see, because the annealing time influences only the mean particle radius; all other parameters are scale invariant and independent of the current annealing time. In particular, this implies that all characteristics of model microstructures are self-similar, not only the distribution of particle radii.

5. Model fitting and validation

In previous sections, we described the processing and segmentation of experimental data and our approach to stochastic modeling. The dynamic stochastic model is based on a (static) 3D model and a time function that maps the coarsening state to the model parameters. By construction, this model evolves in a self-similar manner. In this section, we fit the proposed dynamic model to experimental (time-resolved) data. Subsequently, we validate the dynamic model by means of various characteristics estimated from experimental and simulated data; as part of the validation process we also consider experimental time steps that were not used in model fitting.

5.1. Fitting of dynamic model

The dynamic model consists of a random 3D tessellation, the parameters of which are computed from a time function that assumes power-law grain growth. We assume that coarsening is diffusion controlled in our experimental system, which leads to a scaling exponent $n = 3$ [19]. Therefore, we fit only the parameters k and $\bar{R}(0)$ in Eq. (1) to our experimentally obtained mean grain sizes. Then, we estimate values for the parameters c_μ, c_σ, s_{hc} and d that are required to obtain the desired grain sizes and grain shapes from the 3D model.

The power-law growth formula with fixed $n = 3$ is a function of the parameters $k > 0$ and $\bar{R}(0) > 0$, in which k describes the coarsening dynamics and $\bar{R}(0)$ the mean grain radius at time $t = 0$. First, we compute estimates $\widehat{\bar{R}}(t)$ of the mean radii $\bar{R}(t)$ for $t \in T$ from experimental data sets. Then, we perform parameter regression by minimizing the sum of squared errors, *i.e.*,

$$\begin{pmatrix} \widehat{k} \\ \widehat{\bar{R}}(0) \end{pmatrix} = \underset{(k,\bar{R}(0))^T \in \mathbb{R}^+ \times \mathbb{R}^+}{\arg\min} \sum_{t \in T} \left(\widehat{\bar{R}}(t) - \sqrt[3]{\bar{R}^3(0) + k \cdot t}\right)^2 .$$

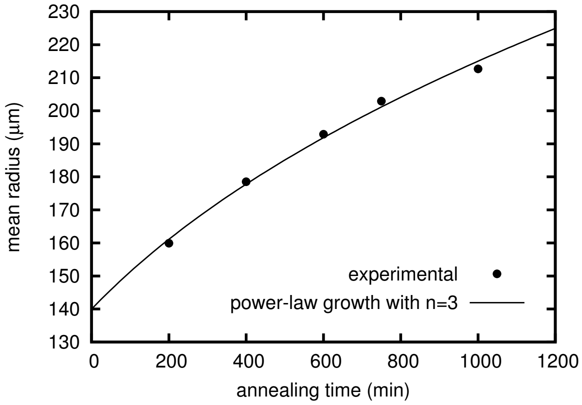

Figure 7. Power-law growth of mean cell radii: points from experimental data and fitted function.

This non-linear function is minimized using the Levenberg-Marquardt algorithm [61,62]. Experimental mean radii and the fitted power-law growth function are displayed in Figure 7. Note that we consider only the time steps $t \in T = \{200, 400, 600, 750, 1000\}$ during model fitting. The time step $t = 900$ will be used for validation purposes. The minimization procedure yields the estimates $\widehat{k} = 7197.3\,(\mu\text{m})^3/\text{s}$ and $\widehat{\overline{R}}(0) = 139.95\,\mu\text{m}$ for the parameters of the power-law growth formula.

To obtain values for the remaining parameters, $c_\mu > 0$, $c_\sigma > 0$, $s_{\text{hc}} \in (0, 1]$ and $d > 0$, we make use of so-called *minimum-contrast estimation* [51]. The latter technique determines optimal parameter values by traversing the (discretized) parameter space P (see Table 2) and evaluating the goodness-of-fit using a *contrast function*. The contrast function defines a certain distance between experimental and simulated data, usually by comparing some characteristics. In our case, we choose to optimize the fit of the cell size distribution for all time steps $t \in T$ at once. Therefore, the values of the parameters c_μ, c_σ, s_{hc} and d are estimated by solving the following minimization problem:

$$\begin{pmatrix} \widehat{c_\mu} \\ \widehat{c_\sigma} \\ \widehat{s_{\text{hc}}} \\ \widehat{d} \end{pmatrix} = \underset{(c_\mu, c_\sigma, s_{\text{hc}}, d) \in P}{\arg\min} \sum_{t \in T} \int_0^\infty \left(\widehat{F}_R^{(t)}(r) - F_R^{(t)}(r) \right)^2 \mathrm{d}r \,,$$

where $\widehat{F}_R^{(t)}(r)$ denotes the (empirical) cumulative distribution function of volume-equivalent radii of grain regions at time t, and $F_R^{(t)}(r)$ denotes the cumulative distribution function of volume-equivalent radii of Laguerre cells at time t, which depends on the vector $(c_\mu, c_\sigma, s_{\text{hc}}, d)$. Note that the cumulative distribution functions are estimated from interior cells only; that is, any grains touching the surface of the (real or simulated) sample are ignored.

The discretized parameter space P and the values of the parameters c_μ, c_σ, s_{hc} and d that were obtained by minimum-contrast estimation are quoted in Table 2. The optimal parameter values are interesting in their own right: without having imposed

Table 2. Discretized parameter space for minimum-contrast estimation and the resulting optimal parameter values.

parameter	min	max	step	constraint	optimal
c_μ	0.7	1.3	0.02		1.0
c_σ	0.25	0.5	0.05		0.4
s_{hc}	0.7	1.0	0.05		0.85
d	0.55	1.25	0.05	$d_{\mathrm{hc}} = d \cdot s_{\mathrm{hc}}^3 < 0.65$	1.0

Table 3. Mean values and standard deviations of characteristics at $t = 900\,\mathrm{min}$. (This time step was not considered during model fitting.)

	experimental data		simulated data	
	mean	sd	mean	sd
cell radius	$210.5\,\mu$m	$77.4\,\mu$m	$206.8\,\mu$m	$81.0\,\mu$m
number of faces	13.2	4.4	13.2	5.1
number of edges	33.7	13.1	33.7	15.3
sphericity	0.84	0.06	0.83	0.10
$\sqrt{\text{face area}}$	$217.6\,\mu$m	$98.6\,\mu$m	$209.4\,\mu$m	$97.9\,\mu$m
edge length	$174.7\,\mu$m	$99.4\,\mu$m	$165.7\,\mu$m	$94.1\,\mu$m

such a condition explicitly, we obtained the result that the collective volume of all spheres is identical to that of the overall simulation window ($d = 1$), which also means that the cell volumes of the Laguerre tessellation are good approximations to the corresponding volumes of the spheres used as seed points, leading to $c_\mu \approx 1$.

5.2. Model validation

After fitting the proposed model to experimental data, we validate the model by assessing the extent to which it captures the microstructures observed in experiment. To evaluate the quality of the model fit, we compare various characteristics estimated from experimental data and model realizations. Edge effects are reduced by omitting grains touching the sample surface. In the following, we choose the time steps $t = 400$, 600 and 900 min for visualization of characteristics in figures. Note that $t = 900\,\mathrm{min}$ is a time step that was not used during fitting to determine optimal model parameters. A 3D visualization of the data is provided by the cylindrical cut-outs shown in Figure 8. For $t = 900\,\mathrm{min}$, Table 3 illustrates the excellent agreement that was obtained between experiment and model for the mean values and standard deviations of several characteristics of the microstructure.

We now examine distributions of these microstructural characteristics, which contain more information than only the first and second moments. Figure 9 shows distributions for the normalized cell radius and the number of cell neighbors, plotted using the corresponding density functions. We see that the 96% point-wise confidence band for the normalized cell radius and the number of cell faces matches the experimental

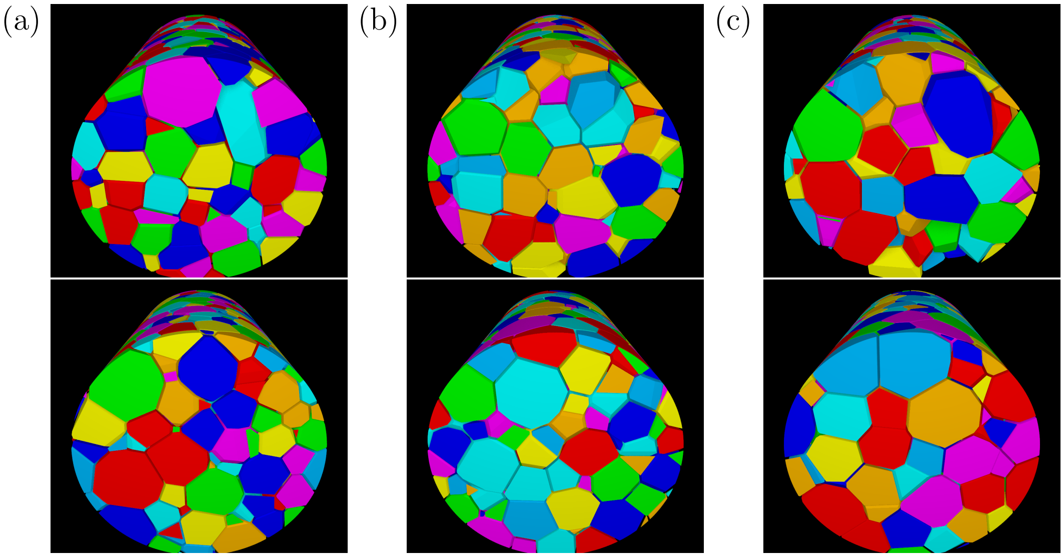

Figure 8. Small cylindrical regions cut out of 3D microstructures extracted from (top) experimental data and (bottom) model realizations at (a) $t = 400$, (b) $t = 600$ and (c) $t = 900\,\text{min}$.

data nearly perfectly. Variations in experimental data from time step to time step have several possible sources. First, it is possible that the system has not yet reached the state of self-similar evolution. However, as discussed in Section 2, we assume that all characteristics lie within the range of statistical uncertainty about their steady-state values. Second, the number of observed grains decreases steadily. Later points in time correspond to larger and, therefore, fewer grains in the cylindrical sample, which leads to an increase in statistical fluctuations and to a growing influence of the sample surface (*i.e.* edge effects): there are 1011 grains at $t = 400$ min, 765 grains at $t = 600$ min, and 547 grains at $t = 900$ min (counting performed after removal of grains in contact with the sample surface). From the excellent agreement evident in Figure 9(a) with respect to the measured and simulated normalized grain size distributions—combined with the close match between mean grain and cell radii shown in Figure 7—we conclude that our model correctly reproduces the non-normalized grain size distribution at each time step. In turn, this implies that the model accurately captures the total number of (interior) grains, as well.

Another important characteristic is the shape of the cells. To evaluate the shape, we computed the *cell sphericity* [63]. Sphericity is defined as the ratio of the surface area of the volume-equivalent sphere to the surface area of the corresponding grain or cell. High values for this ratio imply that the shape is quite similar to that of a sphere, whereas small values signify larger discrepancies—*e.g.* the true shape could be elongated in a particular direction. Figure 10(a) shows the density functions estimated for cells obtained from the fitted dynamic model and from convex polyhedra extracted from experimental data. The shapes of the distributions do not coincide perfectly, but they are fairly close together, and their values for expectation and variance are quite

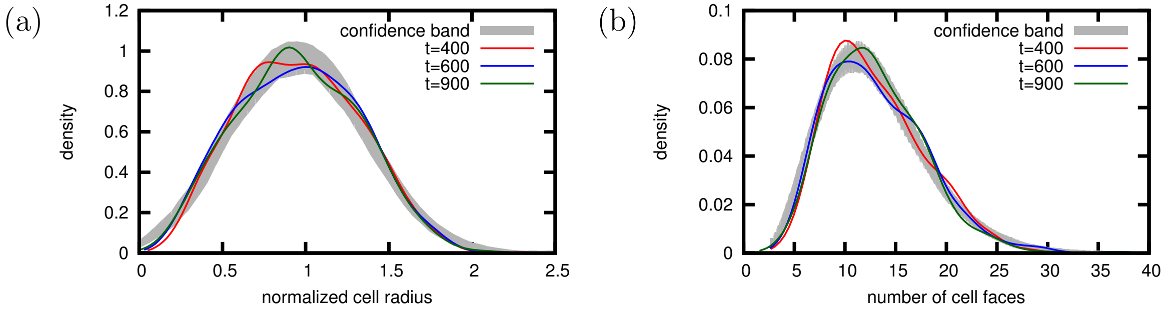

Figure 9. Plots of the density function of the distributions of the (a) normalized cell radius and (b) number of cell neighbors. The curves correspond to experimental data, whereas the gray shading denotes the 96% point-wise confidence bands of the dynamic model. Note that the confidence bands are quite similar for all time steps (and theoretically identical) due to self-similarity.

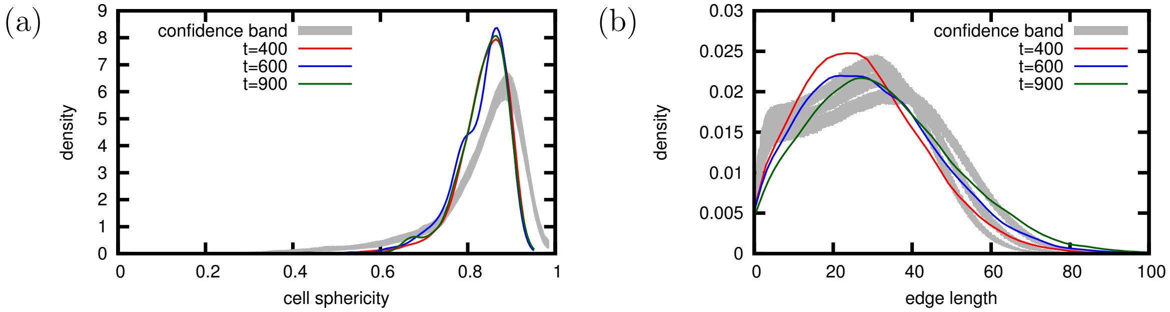

Figure 10. Plots of the density function of the distributions of (a) cell sphericity and (b) edge lengths. The curves correspond to experimental data, whereas the gray shading denotes the 96% point-wise confidence bands of the dynamic model.

similar. The same is true for the distribution of cell edge lengths (Figure 10(b)).

Although radius, number of neighbors, sphericity and edge lengths are the most important characteristics, we evaluated further characteristics, as well, including the distribution of face areas, the number of edges per cell and 2D joint distributions of quantities like the cell radius and sphericity. To assess spatial dependencies, we looked at pair and mark correlation functions [52] of cell centroids (with volume-equivalent radius as the mark) and the correlation of cell sizes with neighborhood degree (*i.e.,* direct neighbors, indirect neighbors with the shortest path crossing through one, two or more cells). The pair and mark correlation of centroids were found to be strongly influenced by the packing of cells and their size distribution; therefore, these characteristics are not very meaningful. With respect to the neighborhood degree, it is somewhat surprising that we observed no correlation between cell sizes, even for direct neighbors.

6. Conclusions

In this paper we presented a dynamic stochastic simulation model for 3D particle microstructures undergoing the coarsening phenomenon known as Ostwald ripening.

We analyzed time series of 3D images that were recorded *in situ* in polycrystalline Al-Cu alloys manifesting an ultra-high volume fraction of the coarsening (Al-rich) phase. Using this information we developed a dynamic model for the 3D morphology of the coarsening grains at arbitrary time steps. Our stochastic approach is based on random Laguerre tessellations and is by definition self-similar—*i.e.,* it depends only on the mean grain radius, which in turn can be estimated at each point in time. Our validation of the model shows that it provides a faithful representation of the statistical features of the experimental data, even for time steps not used in the model fitting. This is rather surprising, given that the model contains only three scalar parameters that influence grain size and shape. Furthermore, we conclude that self-similarity is a reasonable assumption for this particular set of experimental data—not only for the particle size distribution, but also for the complete 3D morphology. To our knowledge, this is the first discussion of *systematic* self-similarity—a feature that can be established with the help of stochastic models—for microstructures generated by Ostwald ripening, which is more general than looking at the scaling behavior of individual structural characteristics.

In the future, it would be interesting to fit our dynamic model to additional samples having comparable as well as different values for V_V. In principle, the only model parameters that depend on the constituent materials of a given specimen are the power-law parameters describing the growth of the mean grain size. The (scale-invariant) 3D morphology—and the corresponding parameter values—ought to be similar for all samples sharing the same volume fraction of a solid coarsening phase embedded in a liquid matrix. If this supposition proves to be true, then our proposed model would be able to predict the full 3D morphology for a wide range of Ostwald ripening scenarios, provided the model parameters have been calibrated against V_V. Furthermore, we intend to develop a “full” 4D model in which dynamics are integrated not only at the statistical level but also at the level of individual grains. In particular, we plan to employ the particle tracking algorithm presented in [18] to capture the dynamics of individual grains in a stochastic model. For the evolution of individual grains, the local neighborhood is important, as the configuration of nearby grains has a strong effect on whether a given grain loses or gains volume. Such effects will be incorporated into the 4D model based on a statistical analysis of local grain environments in experimental data.

Acknowledgements

The authors are grateful to D. Molodov of the Institute of Physical Metallurgy and Metal Physics, RWTH Aachen, for sample preparation and to M. Scheel (ESRF) and L. Helfen (ESRF and the Institute for Photon Science and Synchrotron Radiation of KIT) for extensive technical support during synchrotron measurements. Partial support for this work was provided by the Deutsche Forschungsgemeinschaft through NSF/DFG Materials World Network Projects KR 1658/4-1 and OD 18/14-1.

References

[1] P. W. Voorhees. The theory of Ostwald ripening. *Journal of Statistical Physics*, 38:231–252, 1985.

[2] P. W. Voorhees. Ostwald ripening of two-phase mixtures. *Annual Review of Materials Science*, 22:197–215, 1992.

[3] L. Ratke and P. W. Voorhees. *Growth and Coarsening: Ostwald Ripening in Material Processing.* Springer, Heidelberg, 2002.

[4] A. Baldan. Progress in Ostwald ripening theories and their applications to nickel-base superalloys - Part I: Ostwald ripening theories. *Journal of Materials Science*, 37:2171–2202, 2002.

[5] K. G. Wang, M. E. Glicksman, and K. Rajan. Length scales in phase coarsening: Theory, simulation, and experiment. *Computational Materials Science*, 34(3):235–253, 2005.

[6] K. G. Wang and M. E. Glicksman. Chap. 5: Ostwald ripening in materials processing. In J. R. Groza, J. F. Shackelford, E. J. Lavernia, and M. T. Powers, editors, *Materials Processing Handbook*. CRC Press, Boca Raton, 2007.

[7] I. M. Lifshitz and V. V. Slyozov. The kinetics of precipitation from supersaturated solid solutions. *Journal of Physics and Chemistry of Solids*, 19(1–2):35–50, 1961.

[8] C. Wagner. Theorie der Alterung von Niederschlägen durch Umlösen (Ostwald-Reifung). *Zeitschrift für Elektrochemie*, 65(7):581–591, 1961.

[9] P. W. Voorhees and M. E. Glicksman. Ostwald ripening during liquid phase sintering—Effect of volume fraction on coarsening kinetics. *Metallurgical Transactions A*, 15(6):1081–1088, 1984.

[10] N. Akaiwa and P. W. Voorhees. Late-stage phase separation: Dynamics, spatial correlations, and structure functions. *Physical Review E*, 49:3860–3880, 1994.

[11] K. G. Wang, M. E. Glicksman, and C. Lou. Correlations and fluctuations in phase coarsening. *Physical Review E*, 73:061502, 2006.

[12] S. P. Marsh and M. E. Glicksman. Kinetics of phase coarsening in dense systems. *Acta Materialia*, 44:3761–3771, 1996.

[13] S. P. Marsh and M. E. Glicksman. Ostwald ripening in non-spherical morphologies. *Materials Science and Engineering A*, 238(1):140–147, 1997.

[14] R. T. DeHoff and C. V. Iswaran. The usefulness of integral mean curvature measurements in the study of the kinetics of coarsening. *Metallurgical Transactions A*, 13(8):1389–1395, 1982.

[15] S. C. Hardy and P. W. Voorhees. Ostwald ripening in a system with a high volume fraction of coarsening phase. *Metallurgical and Materials Transactions A*, 19:2713–2721, 1988.

[16] D. J. Rowenhorst, J. P. Kuang, K. Thornton, and P. W. Voorhees. Three-dimensional analysis of particle coarsening in high volume fraction solid-liquid mixtures. *Acta Materialia*, 54:2027–2039, 2006.

[17] N. Limodin, L. Salvo, M. Suéry, and M. DiMichiel. In situ investigation by X-ray tomography of the overall and local microstructural changes occurring during partial remelting of an Al–15.8 wt.% Cu alloy. *Acta Materialia*, 55:3177–3191, 2007.

[18] T. Werz, M. Baumann, U. Wolfram, and C. E. Krill III. Particle tracking during Ostwald ripening using time-resolved laboratory X-ray microtomography. *Materials Characterization*, 90:185–195, 2014.

[19] K. G. Wang, X. Ding, K. Chang, and L. Q. Chen. Phase-field simulation of phase coarsening at ultrahigh volume fractions. *Journal of Applied Physics*, 107:061801, 2010.

[20] S. G. Kim. Large-scale three-dimensional simulation of Ostwald ripening. *Acta Materialia*, 55:6513–6525, 2007.

[21] D. Fan, S. P. Chen, L.-Q. Chen, and P. W. Voorhees. Phase-field simulation of 2-D Ostwald ripening in the high volume fraction regime. *Acta Materialia*, 50(8):1895–1907, 2002.

[22] A. Luque, J. Aldazabal, J. M. Martinez-Esnaola, A. Martin-Meizoso, J. G. Sevillano, and R. S. Farr. Diffusional Monte Carlo model of liquid-phase sintering. *Mathematics and Computers in Simulation*, 81:2564–2580, 2011.

[23] P. Streitenberger. Analytical description of phase coarsening at high volume fraction. *Acta*

Materialia, 61:5026–5035, 2013.

[24] J. Svoboda and F. D. Fischer. Generalization of the Lifshitz–Slyozov–Wagner coarsening theory to non-dilute multi-component systems. *Acta Materialia*, 79:304–314, 2014.

[25] J.H. Panchal, S.R. Kalidindi, and D.L. McDowell. Key computational modeling issues in Integrated Computational Materials Engineering. *Computer-Aided Design*, 45(1):4–25, 2013.

[26] W. Bender and L. Ratke. Ostwald ripening of liquid phase sintered Cu-Co dispersions at high volume fractions. *Acta Materialia*, 46:1125–1133, 1998.

[27] S. S. Kang and D. N. Yoon. Kinetics of grain coarsening during sintering of Co-Cu and Fe-Cu Alloys with low liquid contents. *Metallurgical and Materials Transactions A*, 13(8):1405–1411, 1982.

[28] S. K. Kailasam, M. E. Glicksman, S. S. Mani, and V. E. Fradkov. Investigation of microstructural coarsening in Sn-Pb alloys. *Metallurgical and Materials Transactions A*, 30(6):1541–1547, 1999.

[29] K. G. Wang and H. Yan. Simulating three-dimensional phase coarsening at ultrahigh volume fractions by phase-field method. *Solid State Phenomena*, 172-174:1112–1118, 2011.

[30] M.K. Chen and P.W. Voorhees. The dynamics of transient Ostwald ripening. *Modelling and Simulation in Materials Science and Engineering*, 1:591–612, 1993.

[31] V. A. Snyder, J. Alkemper, and P. W. Voorhees. Transient Ostwald ripening and the disagreement between steady-state coarsening theory and experiment. *Acta Materialia*, 49(4):699–709, 2001.

[32] J. C. Russ. *The Image Processing Handbook*. CRC Press, Boca Raton, 5th edition, 2007.

[33] B. Jähne. *Digital Image Processing*. Springer, Berlin, 6th revised and extended edition, 2005.

[34] S. Beucher and C. Lantuéjoul. Use of watersheds in contour detection. In *Proceedings of the International Workshop on Image Processing, Real-Time Edge and Motion Detection/Estimation*, Rennes, France, 1979.

[35] S. Beucher and F. Meyer. The morphological approach to segmentation: the watershed transformation. In E.R. Dougherty, editor, *Mathematical Morphology in Image Processing*, pages 433–481. Marcel Dekker, New York, 1993.

[36] J. B. T. M. Roerdink and A. Meijster. The watershed transform: definitions, algorithms, and parallellization strategies. *Fundamenta Informaticae*, 41:187–228, 2001.

[37] R. Beare and G. Lehmann. The watershed transform in ITK - discussion and new developments. *The Insight Journal*, June 2006. Paper ID: 92.

[38] T. B. Massalski. *Binary Alloy Phase Diagrams - AlCu phase diagram*, volume 1. ASM, Providence, 3rd edition, pages 141–143, 1996.

[39] A. Lyckegaard, G. Johnson, and P. Tafforeau. Correction of ring artifacts in X-ray tomographic images. *International Journal of Tomography and Statistics*, 18(F11):1–9, 2011.

[40] J. Hoshen and R. Kopelman. Percolation and cluster distribution. I. Cluster multiple labeling technique and critical concentration algorithm. *Physical Review B*, 14:3438–3445, 1976.

[41] A. Spettl, T. Werz, C.E. Krill III, and V. Schmidt. Parametric representation of 3D grain ensembles in polycrystalline microstructures. *Journal of Statistical Physics*, 154:913–928, 2014.

[42] C. Lautensack. *Random Laguerre Tessellations*. PhD thesis, Universität Karlsruhe, Weiler bei Bingen, 2007.

[43] A. Okabe, B. Boots, K. Sugihara, and S. N. Chiu. *Spatial Tessellations: Concepts and Applications of Voronoi Diagrams*. J. Wiley & Sons, Chichester, 2nd edition, 2000.

[44] Z. Fan, Y. Wu, X. Zhao, and Y. Lu. Simulation of polycrystalline structure with Voronoi diagram in Laguerre geometry based on random closed packing of spheres. *Computational Materials Science*, 29:301–308, 2004.

[45] H. Telley, T.M. Liebling, A. Mocellin, and F. Righetti. Simulating and modelling grain growth as the motion of a weighted Voronoi diagram. *Materials Science Forum*, 94–96:301–306, 1992.

[46] H. Telley, T. M. Liebling, and A. Mocellin. The Laguerre model of grain growth in two dimensions: I. Cellular structures viewed as dynamical Laguerre tessellations. *Philosophical Magazine Part B*, 73(3):395–408, 1996.

[47] H. Telley, T. M. Liebling, and A. Mocellin. The Laguerre model of grain growth in two dimensions:

II. Examples of coarsening simulations. *Philosophical Magazine Part B*, 73(3):409–427, 1996.

[48] X. Xue, F. Righetti, H. Telley, and T. M. Liebling. The Laguerre model for grain growth in three dimensions. *Philosophical Magazine Part B*, 75(4):567–585, 1997.

[49] C. Lautensack and T. Sych. 3D image analysis of open foams using random tessellations. *Image Analysis & Stereology*, 25:87–93, 2006.

[50] C. Lautensack. Fitting three-dimensional Laguerre tessellations to foam structures. *Journal of Applied Statistics*, 35(9):985–995, 2008.

[51] J. Illian, A. Penttinen, H. Stoyan, and D. Stoyan. *Statistical Analysis and Modelling of Spatial Point Patterns*. J. Wiley & Sons, Chichester, 2008.

[52] S. N. Chiu, D. Stoyan, W. S. Kendall, and J. Mecke. *Stochastic Geometry and its Applications*. J. Wiley & Sons, Chichester, 3rd edition, 2013.

[53] D. J. Daley and D. Vere-Jones. *An Introduction to the Theory of Point Processes, Volume I: Elementary Theory and Methods*. Springer, New York, 2nd edition, 2003.

[54] D. J. Daley and D. Vere-Jones. *An Introduction to the Theory of Point Processes, Volume II: General Theory and Structure*. Springer, New York, 2nd edition, 2008.

[55] K. Schladitz, C. Redenbach, T. Sych, and M. Godehardt. Model based estimation of geometric characteristics of open foams. *Methodology and Computing in Applied Probability*, 14:1011–1032, 2012.

[56] D. Stoyan. Simulation and characterization of random systems of hard particles. *Image Analysis & Stereology*, 21:S41–S48, 2002.

[57] J. Mościński, M. Bargieł, Z. A. Rycerz, and P. W. M. Jacobs. The force-biased algorithm for the irregular close packing of equal hard spheres. *Molecular Simulation*, 3(4):201–212, 1989.

[58] A. Bezrukov, M. Bargieł, and D. Stoyan. Statistical analysis of simulated random packings of spheres. *Particle & Particle Systems Characterization*, 19(2):111–118, 2002.

[59] C. Hirsch, G. Gaiselmann, and V. Schmidt. Asymptotic properties of collective-rearrangement algorithms. *ESAIM: Probability and Statistics*, DOI: 10.1051/ps/2014026, 2015.

[60] M. Fátima Vaz and M. A. Fortes. Grain size distribution: The lognormal and the gamma distribution functions. *Scripta Metallurgica*, 22(1):35–40, 1988.

[61] K. Levenberg. A method for the solution of certain non-linear problems in least squares. *Quarterly of Applied Mathematics*, 2:164–168, 1944.

[62] D. W. Marquardt. An algorithm for least-squares estimation of nonlinear parameters. *Journal of the Society for Industrial and Applied Mathematics*, 11(2):431–441, 1963.

[63] H. Wadell. Volume, shape and roundness of quartz particles. *Journal of Geology*, 43(3):250–280, 1935.